Structural evolution at short and medium range distances during crystallization of a P2O5-Li2O-Al2O3-SiO2 glass

Pauline Glatz, Monique Comte, Lionel Montagne, Bertrand Doumert, Fabrice Cousin, Laurent Cormier

Structural evolution at short and medium range distances during crystallization of a P_2O_5-Li_2O-Al_2O_3-SiO_2 glass

Pauline Glatz[1,2,3], Monique Comte[1], Lionel Montagne,[2], Bertrand Doumert[4], Fabrice Cousin[5], Laurent Cormier[3]

[1]Corning European Technology Center, 7 Bis Avenue de Valvins, 77210 Avon-France

[2]Univ. Lille, CNRS, Centrale Lille, ENSCL, Univ. Artois, UMR 8181 - UCCS - Unité de Catalyse et Chimie du Solide, F-59000 Lille, France

[3]Sorbonne Université, CNRS, Museum National d'Histoire Naturelle, IRD, Institut de Minéralogie, de Physique des Matériaux et de Cosmochimie (IMPMC), UMR 7590, 4 place Jussieu, 75005 Paris, France

[4]Univ. Lille, CNRS, INRA, Centrale Lille, ENSCL, Univ. Artois, FR 2638 - IMEC - Institut Michel-Eugène Chevreul, F-59000 Lille, France

[5]LLB - CNRS UMR 12 - Laboratoire Léon Brillouin, Saclay, France

*

E-mail: laurent.cormier@sorbonne-universite.fr

Abstract

Li_2O-Al_2O_3-SiO_2 (LAS) glass-ceramics have important industrial applications and bulk nucleation is usually achieved by using nucleating agents. In particular, P_2O_5 is an efficient agent in glasses containing a low level of Al_2O_3 but its role in the first stages of nucleation is not well established. In this study, we combine structural investigations from local to mesoscales to describe the structural evolution during crystallization of LAS glass-ceramics. Local environment is probed using ^{29}Si and ^{31}P MAS-NMR, indicating organization of P in poorly crystallized Li_3PO_4 species prior any crystallization. To better understand the detailed nanoscale changes of the glass structure, ^{31}P-^{31}P DQ-DRENAR homo-nuclear correlation experiments have been carried out, revealing the gradual segregation of P atoms associated with the formation of disordered Li_3PO_4. Small-angle neutron scattering data also show the apparition of nanoscale heterogeneities associated with Li_3PO_4 species upon heating treatments and allow the determination of their average sizes. These new structural information enhance our understanding of the P role in nucleation mechanisms. Nucleation is initiated by gradual change in P environment implying P segregation upon heating treatments, forming disordered Li_3PO_4 heterogeneities. The segregation of P atoms enables the precipitation of meta- and di-silicate phases.

1 Introduction

The incorporation of specific oxides, known as nucleating agents, in the glass melt strongly influences nucleation and crystal growth. It is actually the best technical route to tailor glass-ceramics with desired properties (transparency, optical, mechanical, thermal ...) for industrial applications.[1] The mechanism of how nucleating agent favors nucleation is still debated but major recent advances have clarified their role, particularly for TiO_2 and ZrO_2 in various aluminosilicate glasses. From heterogeneities or amorphous phase separation preexisting in the as-cast glasses,[2-4] the agents precipitate heterogeneously upon heat treatments, leading to structural and compositional modifications of the glass that allow nucleation of a major phase.[4-8]

Though TiO_2 and ZrO_2 are the most commonly used nucleating agents, P_2O_5 has been well recognized to aid nucleation in various silicate glasses[9-13] and is particularly effective when introduced to LiO_2-SiO_2 glasses.[5-13] Deep insights on the role of P_2O_5 have been mostly obtained using NMR techniques, showing that P_2O_5 can precipitate as a phosphate phase, usually Li_3PO_4, but this phase is not considered as a precursor for the nucleation of $Li_2Si_2O_5$.[13] Indeed, a first step in the nucleation mechanisms has been recently proposed with the formation of poorly crystallized Li_3PO_4 prior any crystallization.[14-16] P_2O_5 is also well documented to promote phase separation,[13,17,18] but there is yet no direct confirmation of a relationship between the disordered Li_3PO_4 and any phase separation or any heterogeneities.

Though transmission electron microscopy could be used to investigate phase separation and the early stages of nucleation, amorphous phase separation is sometimes undetectable in these glasses and Li_3PO_4 crystals are unstable under the electron beam and difficult to observe.[19] An alternative technique is small-angle scattering, which is widely used to detect phase separation and follow nucleation and growth processes.[18,20-24] In particular, due to the good contrast in neutron scattering lengths between P and other components in lithium

silicate glasses, small-angle neutron scattering (SANS) is advantageous.[25]

Advanced solid-state ^{31}P NMR techniques have been recently developed to characterize the medium range order in glasses, revealing nanometric-sized chemical and structural heterogeneities corresponding to clusters of PO_4 tetrahedra in bioactive glasses.[26-28] DQ-DRENAR (Double-Quantum based Dipolar Recoupling Effects Nuclear Alignment Reduction) has been used to probe the spatial distribution of orthophosphate units and has evidenced their nano-segregation in a lithium silicate glass and glass-ceramics.[29]

In this paper, we investigate whether heterogeneities related to the presence of P_2O_5 are observable in glasses or whether changes appear with thermal treatments. To complement local changes previously observed,[14-16] transmission electron microscopy (TEM), Small-Angle Neutron Scattering (SANS) and correlation technique ^{31}P-^{31}P DQ-DRENAR were used to probe medium range distance (1 nm-2 nm) and mesoscale microstructure in a Li_2O-Al_2O_2-SiO_2 (LAS) glass containing 1 mol% P_2O_5.

2 Experimental Section

2.1 Materials

Glasses in the Li_2O-Al_2O_3-SiO_2 ternary system with 0 and 1 mol% P_2O_5 were prepared as reported previously.[16] The P_2O_5 content was chosen to avoid phase separation that we have observed for $P_2O_5 \geq 3$ mol%. Analytical grade reagents Li_2CO_3 (Sigma Aldrich, 99%), Al_2O_3 (Merck, 99.9%), SiO_2 (Alfa Aesar, 99.5%) and $(NH_4)_2HPO_4$ (Sigma Aldrich, 98%) were mixed using an agate pestle and mortar, dried and melted in a platinum crucible at 1550°C and maintained 2 h at this temperature. Then the samples were quenched by dipping the bottom of the crucible into water. The glasses were ground and remelted to ensure a good homogeneity. Glasses are transparent and bubble free.

The glass compositions were examined by Electron Probe Micro-Analyser (EPMA, CAMPARIS, Sorbonne Université, Paris, France) with a CAMECA SX-Five apparatus equipped

Table 1: Analyzed compositions (mol%) by EPMA and F-AES of the glasses investigated in this study. Nominal compositions are in parenthesis. Errors are typically less than 0.3% relative on SiO_2, less than 0.7% relative on Al_2O_3, less than 3% relative on P_2O_5 and 2% relative on Li_2O.

Glass	SiO_2	Al_2O_3	Li_2O	P_2O_5
LAS0.2-P0	75.7 (74.23)	4.6 (4.13)	19.7 (21.64)	0.02 (0.00)
LAS0.2-P1	74.6 (73.47)	4.3 (4.08)	20.2 (21.42)	0.9 (1.02)

with five Wavelength-Dispersive X-ray Spectrometers (WDSs) for SiO_2, Al_2O_3, P_2O_5 and by Flame-Atomic Emission Spectroscopy (F-AES) with a Agilent AA280FS apparatus for Li_2O content. EPMA instrument operates at 15 kV and 10 nA with a spot size of 5 μm. The standards for calibration were orthoclase for silicium and aluminum, and apatite for phosphorus. The nominal and analyzed compositions (averaged over 20 measurements at different points) are reported in Table 1.

2.2 Solid-State NMR

^{29}Si and ^{31}P MAS-NMR (Magic Angle Spinning Nuclear Magnetic Resonance) spectra were acquired using a Bruker AVANCE I solid state spectrometer operating at a magnetic field of 9.4 T. A 7 mm probe and a spinning frequency of 5 kHz were used for ^{29}Si. A 4 mm probe and a spinning frequency of 12.5 kHz were used for ^{31}P. The Larmor frequencies were 79.2 and 161.9 MHz for ^{29}Si and ^{31}P, respectively. For ^{31}P, the pulse durations were 4.8 μs ($\pi/2$) and the recycle delay (rd) were optimized at 140 s to enable enough relaxation and get quantitative spectra. For ^{29}Si, the pulse duration was 2 μs ($\pi/5$), and the rd was 900 s, which is insufficient to enable full relaxation despite its large value; these non-quantitive conditions were used anyway in order to keep acceptable measurement time. The chemical shifts are measured relative to tetramethylsilane (TMS) for ^{29}Si and relative to 85% H_3PO_4 solution for ^{31}P. Spectral decompositions were performed using the DMFIT program,[30] following the procedure explained previously.[31]

In order to get insight on the spatial proximity of similar nuclei (^{31}P) and to obtain the

dipolar coupling constants, a DQ-DRENAR (Double-Quantum, Dipolar Recoupling Effects Nuclear Alignment Reduction) sequence was used, following Ren *et al.*[32] The DQ-DRENAR signal is obtained from two acquisitions. In the first acquisition, the spectrum (S') contains the homonuclear dipolar coupling thanks to the introduction of two C blocks of pulses (two sequences POST-C7 with seven pulses[33]). The signal is thus attenuated by the interaction. In the second acquisition S_0, there are no dipolar couplings due to the out of phase of the two C block pulses, which cancel the dipolar recoupling. These blocks are incremented so that the reinsertion time of the dipolar interaction increases.

The DQ-DRENAR signal is defined by the amplitude S_0-S' that depends on the intensity of the coupling constant between the nuclei, as well as the time during which the coupling is introduced. This time is controlled during the experiment by the term $N.T_r$, where N corresponds to the number of rotation cycles of the rotor and T_r is the rotation period. It is then possible to plot $\frac{S_0-S'}{S_0}$ as a function of $N.T_r$ to get information on the strength of the dipolar coupling and to derive the coupling constants by modeling the curve for $\frac{S_0-S'}{S_0}<0.3$, following the equation:[32]

$$\frac{S_0 - S'}{S_0} = \frac{0.86\pi^2}{15}\left(\sqrt{\sum_k d_{jk}^2}NT_r\right)^2 \tag{1}$$

with d_{jk} the dipolar coupling constant between spins j and k. The closer the phosphorus sites are, the higher the phase shift is and, consequently, the $\frac{S_0-S'}{S_0}$ values will be higher.

The DQ-DRENAR experiments were performed on a Bruker Avance I spectrometer at a magnetic field of 9.4 T with a 4 mm rotor and a speed of 12.5 kHz. A pre-saturation pulse is added to ensure that all acquisitions start with the same magnetization state. A pulse block lasts two rotor periods. The power of the radiofrequency field is optimized so as to have a frequency $\omega_{rf} = 7 * \omega_{rot}$.

2.3 2.4 Small-Angle Neutron Scattering (SANS)

The small-angle neutron scattering (SANS) experiments were carried out on the PAXY spectrometer at the Léon Brillouin Laboratory in CEA Saclay, France.[34] Measurements have been carried out in a q-range of $2.5.10^{-2}$ $nm^{-1} \leq q \leq 5nm^{-1}$ (q=4π sinθ/λ with 2θ the scattering angle and λ the neutron wavelength). To cover these q ranges, four different configurations were used (Table 2).

Table 2: Configurations used in this study: couples (D/λ) for the different q ranges for the two spectrometers

	sample-detector distance D	wavelength λ
very small q	6.7 m	1.5 nm
small q	5 m	0.85 nm
medium q	3.5 m	0.5 nm
large q	1 m	0.5 nm

The samples were polished to the micron on both sides and reduced to a thickness of 1 mm in order to avoid multiple scatterings. Samples are placed in a sample holder between two windows of silica glass. The data were corrected from the background using Cd, from the contribution of empty beam and the contribution from quartz windows, from the detector efficiency using water as a reference sample and then normalized using the scattering cross-section of H_2O for 1mm thickness.

The incoherent scattering (fluctuations in scattering lengths due to nuclear spins) can be neglected as it is q-independent and only the coherent scattering cross-section is considered. The relevant parameter for estimating the probability of an element to scatter neutrons is the coherent scattering length density (SLD) by volume unit, ρ, defined as:

$$\rho = \frac{\sum_{i}^{n} bi}{\nu} \tag{2}$$

with b_i the coherent scattering lengths of atoms i within the elementary scatterer and ν the volume of the elementary scatterer. In Table S1 (Supplementary Materials), the coherent neutron scattering length for the elements used in this study are reported. Due to the negative neutron scattering length of Li and the different scattering length values for P compared to Si and Al, this technique enables the observation of domains that are enriched in Li and P.

Detailed information on SANS formalism can be found in various reviews.[34-36] In a binary system of n rigid and centrosymmetric objects that contains N elementary scatterers homogeneously distributed within a surrounding medium, the measured intensity can be written:

$$I(q)(cm^{-1}) = \frac{nN^2}{V}(\rho_{obj} - \rho_{medium})^2 \nu_{obj}^2 P(q) S(q) \tag{3}$$

with ρ_{obj} et ρ_{medium} the SLD for the objects and the surrounding medium, respectively. V is the sample volume and ν_{obj} is the volume of an elementary scatterer of the object. P(q) is the form factor of the object that contains information about interferences between the elementary scatterers of the object (intra-object correlations) and S(q) is the structure factor that contains information about interference between the centers of gravity of the objects (inter-object correlations).

With the hypothesis that objects are centrosymmetric and well dispersed (no inter-object interactions), S(Q) is equal to 1 in equation 3. The scattered intensity can be described by the Guinier and Porod laws:[35]

$$I(q) = I(0) e^{-\frac{q^2}{3} R_g^2}, \ for \ qR_g < 1 \tag{4}$$

$$I(q) = K_1 + \frac{K_2}{q^4}, \ for \ qR_g > 1 \tag{5}$$

R_g is the radius of gyration. The particle size for spherical objects can be obtained from R_g

with the relationship:

$$R_g = \sqrt{\frac{3}{5}}R \tag{6}$$

When objects are hard spheres of radius R, the form factor can be written:

$$P_{sphre}(q) = \Big[\frac{3sin(qR) - qRcos(qR)}{(qR)^3}\Big]^2 \tag{7}$$

2.4 Transmission Electron Microscopy

Scanning transmission electron microscopy (STEM) was performed in high angle annular dark field imaging mode (STEM-HAADF) using a 2100F microscope operating at 200 kV. This microscope was equipped with a field emission gun and an ultra-high resolution (UHR) pole piece. Samples were ground in agate mortar under acetone and the powder in suspension was collected and deposited on a Cu grid.

2.5 X-ray diffraction

XRD patterns were collected using a X-PERT Pro MPD Panalytical (Almelo, Netherlands) diffractometer on powdered samples. The following configuration was used: Ge[111] monochromator selecting $CuK_{\alpha 1}$ at λ=1.540593 Å for an angular range from 5° to 140° (θ steps of 0.008° and a counting time of 80/,s per step). A real time multiple strip (RTMS) detector X-Celerator operating in scanning mode with an active length of 0.518° was used. Rietveld refinement was performed based on the presence of the following phases: Lithium Di-Silicate ($Li_2Si_2O_5$), JCPDS card N° 04-009-8780; Petalite 1M ($LiAlSi_4O_{10}$), JCPDS card N°04-009-9405; Lithium Meta-Silicate (Li_2SiO_3), JCPDS card N° 00-029-0829; Lithium Phosphate (Li_3PO_4), JCPDS card N° 00-015-0760; α-quartz (SiO_2), JCPDS card N° 01-077-8621. The instrumental resolution file had been determined using the SRM 1976 α-Al_2O_3 XRD standard from NIST. From the Rietveld refinement (Fullproff software code), estimation of phase amounts were extracted.

3 Results

3.1 Comparison of glasses with and without P_2O_5

Figure 1 shows the SANS curves recorded for the glasses with and without P_2O_5, LAS0.2-P1 and LAS0.2-P0, respectively. Error bars have not been added here but the reader can refer to Supplemental Materials (Figure S1). The scattering of the samples when q tends towards 0 is very weak (around 0.05 cm^{-1}). The errors bars are thus very large at the small q values since the contribution from the empty beam has the same order of magnitude as those of samples in this q-range. The two SANS profiles are almost identical, with a very low and nearly flat scattering between 0.2 and 3 nm^{-1}. This indicates that the introduction of P_2O_5 does not create additional scattering. Therefore, according to SANS patterns, the glasses resulting from the melt-quench route are homogeneous.[37]

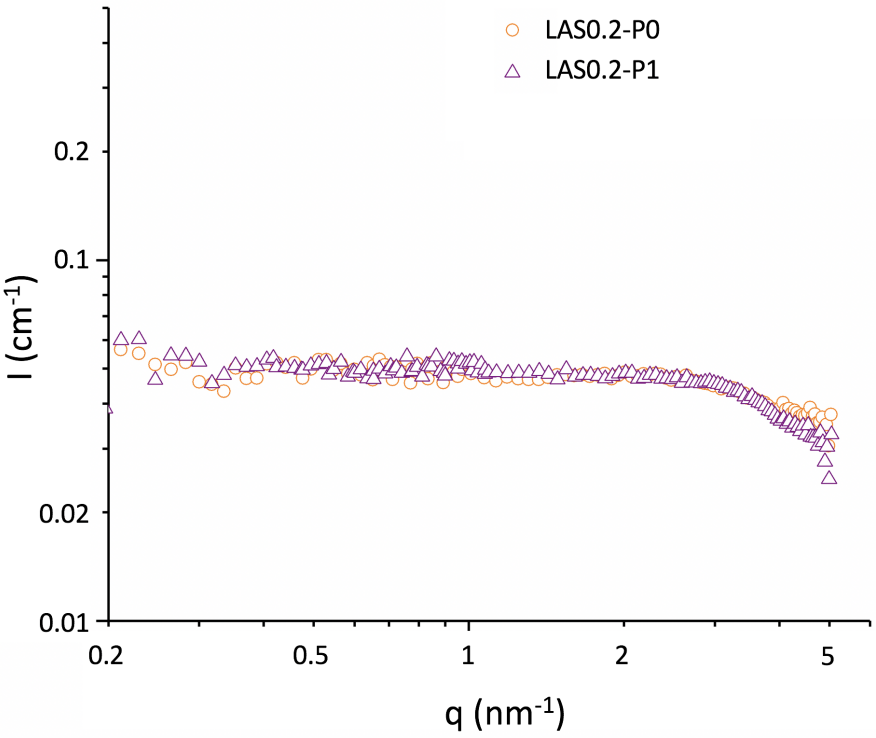

Figure 1: SANS curves of the glasses without P_2O_5 (LAS0.2-P0) and with P_2O_5 (LAS0.2-P1). To improve curve readability, error bars are not shown but can be found in Figure S1.

Using TEM and STEM-HAADF, the LAS0.2-P1 sample appears as an homogeneous glass (Figure 2), consistent also with the absence of macroscopic opalescence. For this composition, the contrast is low because the constituting elements have similar atomic numbers. This may explain the difficulty to observe compositional fluctuations. A good contrast is indeed observed in studies with glasses involving zirconium taking advantage of its high atomic number.[2,3] A study on a glass $72.8SiO_2$ - $20.8Li_2O$ - $2.7Al_2O_3$ - $2.8K_2O$ - $0.8P_2O_5$ - $0.1Sb_2O_3$ (% mol) by Kim et al.[38] is consistent with our observation that no phase separation is detected by TEM.

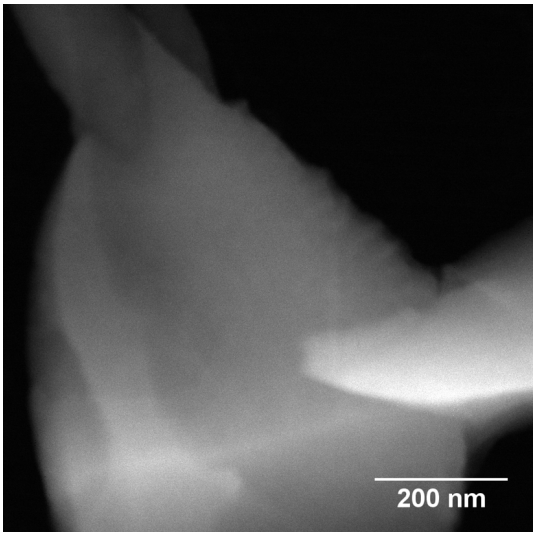

Figure 2: STEM-HAADF image of the LAS0.2-P1 glass.

3.2 Evolution of local environments with heating treatments

Different heating treatments at 525° C, 550° C and 575° C during 1 hour were applied to the LAS0.2-P1 glass. All the samples remained transparent after heat treatments.

3.2.1 X-ray diffraction

X-ray diffractograms are presented in Figure 3a. No Bragg peaks are observed for the as-cast glass or the glasses heat-treated at 525 °C and 550°C. Weak broad peaks are observed at 575°C but the amorphous signal remains dominant. Despite the low intensity of the peaks and their large widths, a Rietveld refinement for the glass heat-treated at 575°C was carried out in order to estimate the amount of the crystallized phases. Results from the refinement are summarized in Table 3. The sample appears mostly amorphous ($\approx 90\%$). As revealed by the broad peak at $\sim 33.3°$, (plane (220) at 33.92°, in the JCPDS 00-015-0760 card), the XRD pattern allows the detection of the γ-Li_3PO_4 phase in very low amount (1 to 2 weight%). XRD analysis (Figure S2) also indicate the presence of lithium metasilicate (LS), lithium disilicate (LS_2) and petalite ($LiAlSi_4O_{10}$).

Table 3: Weight% of phases (relative errors are 5% for amorphous and 8% for crystals) obtained by Rietveld refinement on LAS0.2-P1 heat-treated at 575°C/1h.

Phases	Amorphous	$Li_2Si_2O_5$ (LS_2)	$LiAlSi_4O_{10}$ (P)	Li_2SiO_3 (LS)	Li_3PO_4 (LP)	α-quartz* (a)
weight%	≈ 90	≈ 2	≈ 5	< 0.5	$1 < LP < 2$	< 1

* α-quartz is likely present due to a pollution resulting from the grinding.

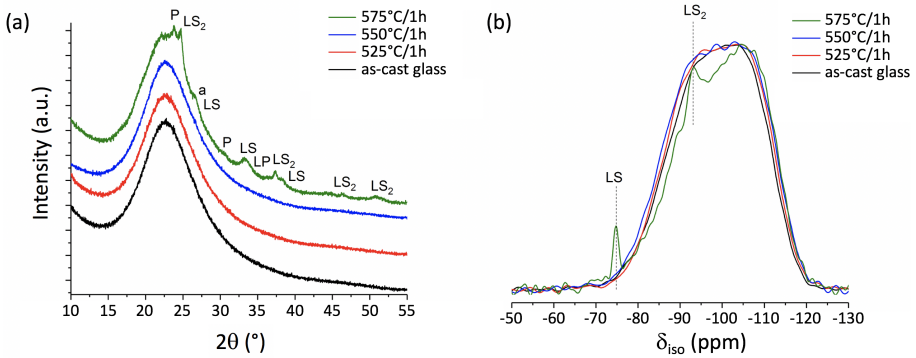

Figure 3: (a) X-ray diffractograms and (b) ^{29}Si MAS-NMR spectra for the as-cast glass LAS0.2-P1 and for samples heat-treated during 1 hour at various temperatures. LS_2: $Li_2Si_2O_5$, LS: Li_2SiO_3, P:$LiAlSi_4O_{10}$, a: α-quartz et LP: Li_3PO_4.

3.2.2 ^{29}Si MAS-NMR

^{29}Si MAS-NMR spectra are shown in Figure 3b. Small changes in the MAS-NMR spectra are visible after the first heating treatments at 525°C and 550°C but they are not significant in terms of the signal/noise ratio for our spectra. At 575°C, resonances at -74.7 ppm and at -93.0 ppm are clearly visible and are assigned to the crystalline phases of lithium metasilicate (at -75 ppm in [39]) and lithium disilicate (at -92.6 ppm in [40]). Their presence is confirmed by XRD (Figure 3a). The petalite phase detected by XRD is not visible on the ^{29}Si spectrum, probably because its relaxation time is very long, as observed for other crystalline silicate phases with large polymerization degree.

To compare with results obtained by XRD, the weight% proportions of each phase were obtained by simulation of the ^{29}Si NMR spectra (Table 4). Note that the recycling time

of 900 seconds does not ensure complete relaxation of the phases and can lead to errors in quantities.

Table 4: Calculation of weight% of lithium metasilicate and disilicate phases for the sample heat-treated at 575°C/1h. Details on the calculation can be found in Table S2. *obtained from the simulation of the ^{29}Si MAS-NMR data.

	Li_2SiO_3	$Li_2Si_2O_5$
% Si within crystals*	2	3
mol% crystalline phases	1.5	1.1
weight% crystalline phases	2.3	2.9

Both methods (NMR and XRD) show that the sample contains Li_2SiO_3 and $Li_2Si_2O_5$ crystals in small quantities (Table 3 and Table 4). However the weight proportions obtained by these two techniques differ. NMR results indicate 2.3 weight% for Li_2SiO_3 while only 0.3 weight% is detected by XRD. Similarly for the $Li_2Si_2O_5$ phase, 2.9 weight% is determined by NMR and 1.8 weight% by XRD. However, quantification is subject to large errors since we are at the detection limits for these two techniques. Moreover, these two techniques can have different sensitivity since ^{29}Si NMR probes local environment and XRD probes coherently scattering domains.

3.2.3 ^{31}P MAS-NMR

The ^{31}P MAS-NMR spectra are presented in figure 4. The spectrum of the as-cast glass is composed of two peaks that are typically lying in the ranges assigned to orthophosphate and pyrophosphate units, i.e. Q^0 and Q^1, respectively. Following the methodology developed in a previous paper,[31] the Q^1 units can be decomposed into two contributions Q^1(0Al) and Q^1(1Al) corresponding to PO_4^{3-} units connected to zero or one Al atom, respectively. The decomposition and the parameters of the various contributions are reported in Table 5. The as-cast glass is obtained with a different batch compared to our previous study.[31] This explains the small differences in the intensities of the contributions and the FWHM, which are close to fitting errors and may also indicate a slightly different thermal history between

the two glass batches.

For the heat-treated samples, in order to fit the main peak at 9.3 ppm (Figure 4), an additional contribution is required, with a FWHM larger at 525°C than at 575°C (see Figure S3 for a typical fit). Due to its relatively large broadness, this resonance has been assigned to a disordered Li_3PO_4 species (disordered-LP) that appears when a heating treatment is applied.[14-16,31] This disordered-LP species is formed at the expense of the Q^0(0Al) and Q^1(0Al) units and occurs before the detection of any crystallization by XRD (Bragg peaks are detected only at 575°C in figure 4). At 550°C, 16% of the phosphorus atoms are in disordered-LP species. At 575°C, a majority of P atoms (52%) in disordered-LP is determined. At this temperature, the peak is narrow, which characterizes a more orderly state than in the case of heating treatments at lower temperatures. The amount of P atoms in disordered-LP corresponds to 0.94 mol% of disordered Li_3PO_4 or 1.9 weight%, which is consistent with XRD results that give 1.7 weight% (Table 3).

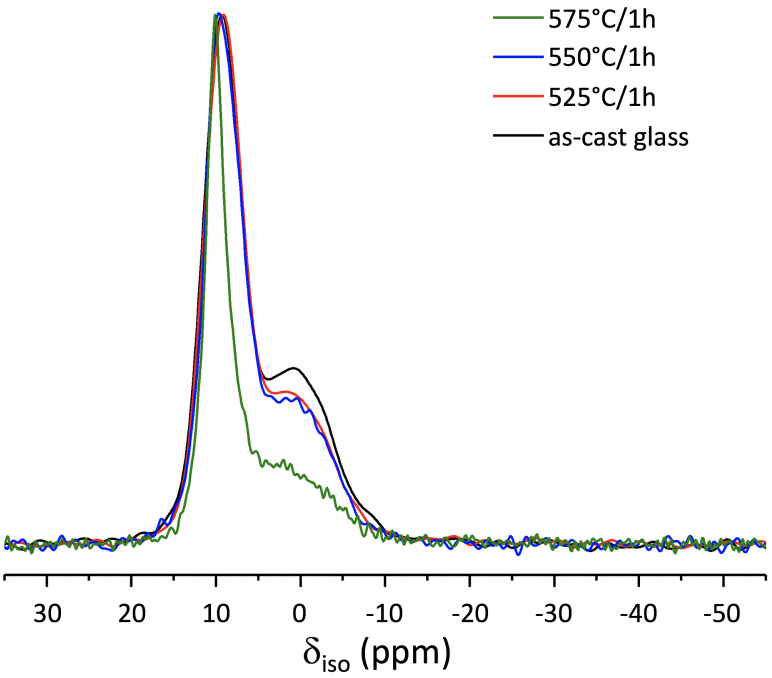

Figure 4: ^{31}P MAS-NMR spectra for the as-cast glass LAS0.2-P1 and for samples heat-treated during 1 hour at various temperatures. The parameters for the different fitted contributions are detailed in Table 5.

Table 5: Isotropic chemical shifts (δ_{iso}), full width at half maximum (FWHM) and relative intensities (I) for the fitted contributions for the as-cast glass LAS0.2-P1 and for samples heat-treated during 1 hour at various temperatures and at 525°C for various times. The gaussian/lorentzian ratios are fixed to 0.80 for all glassy contributions. For the disordered-LP contribution, the ratios are fixed at 0.3 at 525°C and 550°C and at 0.1 at 575°C. The spinning bands are taken into account in the simulation.

sample	disordered-LP			Q^0(0Al)			Q^1(1Al)			Q^1(0Al)		
	δ_{iso} (ppm)	FWHM (ppm)	I (%)	δ_{iso} (ppm)	FWHM (ppm)	I (%)	δ_{iso} (ppm)	FWHM (ppm)	I (%)	δ_{iso} (ppm)	FWHM (ppm)	I (%)
as-cast glass	-	-	-	9.3	5.1	57	3.5	8.0	16	-1.3	8.5	27
525°C 1h	9.5	3.5	8	9.2	5.1	53	3.5	8.0	16	-1.3	8.5	23
525°C 4h	10.1	2.6	16	9.3	5.2	51	3.5	8.0	14	-1.3	8.5	19
550°C 1h	9.8	3.0	16	9.2	5.3	46	3.5	8.0	16	-1.3	8.5	22
575°C 1h	10.1	2.3	52	9.3	5.2	20	3.5	8.0	13	-1.3	8.5	15

Using TEM and STEM-HAADF, the sample heat-treated at 550°C/1 h does not show any crystalline phase nor the development of phase separation (Figure S4). For this heat treatment, the P local environment is modified with the apparition of disordered-LP species (Figure 4) but no Bragg peaks are observed on the X-ray diffraction pattern (Figure 3a). Similarly, no modification has been seen by TEM for a glass $72.8SiO_2$ - $20.8Li_2O$ - $2.7Al_2O_3$ - $2.8K_2O$ - $0.8P_2O_5$ - $0.1Sb_2O_3$ (% mol) heat-treated at 460°C/9 hours.[38] The first changes that have been observed using TEM were after a heat-treatment at 500°C/9 hours, revealing circular zones of 20 nm in diameter, associated with Bragg peaks in the corresponding X-ray diffraction pattern.

3.3 Evolution at mesoscopic scale with heating treatments

3.3.1 SANS

SANS curves obtained for the different thermal treatments are presented in Figure 5 for the LAS0.2-P1 sample heat treated at various temperatures during 1h. There is no change in scattering intensities for the sample heat treated at 525°C/1 h compared to the as-cast glass. Though a small change in the local phosphorus environment has been observed by NMR (Figure 4), any rearrangement at medium range distance is too small to be observed by SANS. At 550°C, a significant change in scattered intensity appears, which is characteristic of a size of scattering objects or a quantity of scattering objects large enough to introduce a neutron contrast with a maximum at about $0.6\,nm^{-1}$. At 575°C, the scattered intensity increases significantly below $1\,nm^{-1}$, indicating that more scattering objects are present. This is due to the appearance of the crystalline phases detected by XRD (Figure 3a). The maximum intensity is progressively shifted to the low q values as the heating temperature treatment increases, which means that the size of scattering objects increases. In Figure S6, the SANS curve is presented for a heating treatment of 1 h at 650°C, for which the scattered intensity is even greater (the sample is more crystallized).

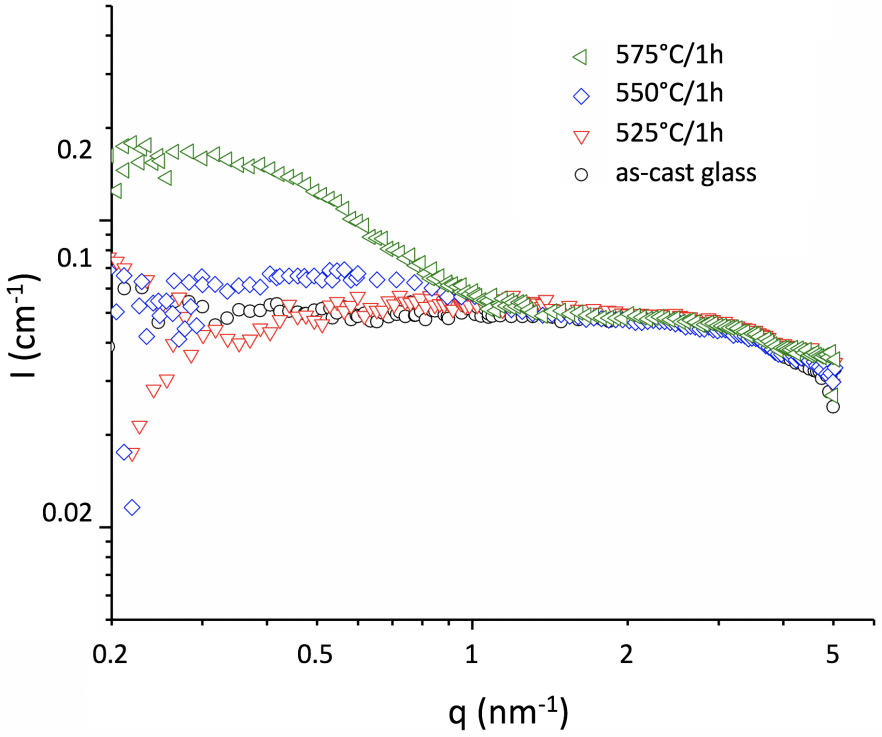

Figure 5: SANS curves for the as-cast glass LAS0.2-P1 and for samples heat-treated during 1 hour at various temperatures. To improve curve readability, error bars are not shown but can be found in Figure S5.

In order to determine the size of the scattering objects observed after thermal treatments, a Guinier analysis (equation 4) was performed for the samples heat-treated at 550°C and 575°C (Figure 6). The scattered intensities were fitted in Guinier's linear domain for $q < 1.25\,nm^{-1}$ for the sample heat-treated at 550°C and $q < 0.687\,nm^{-1}$ for the sample heat-treated at 575°C. The $\ln(I)=f(q^2)$ plots show the linear domains in Figure 6 with a slope that allows the determination of the radius of gyration. No assumption on the shape of the objects is postulated. SasView software has been used for all simulations, using a scale factor to take into account the term $\Delta\rho^2\Phi_{obj}V_{obj}$.

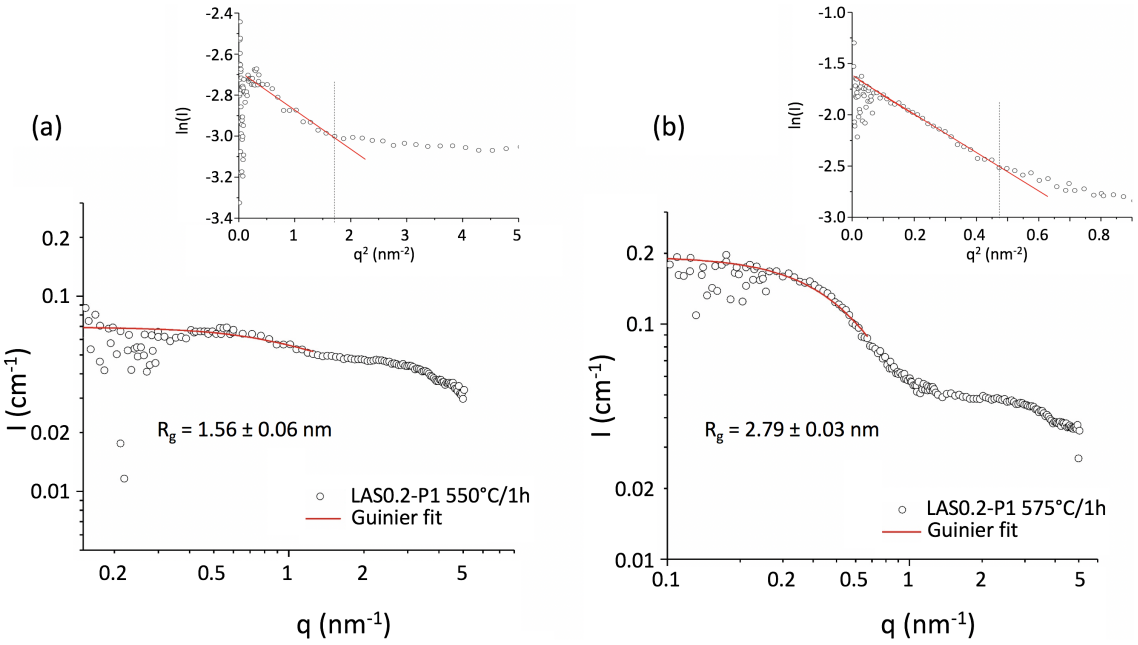

Figure 6: (a) SANS curves (a) LAS0.2-P1 heat-treated at 550°C/1 h (b) LAS0.2-P1 heat-treated at 575°C/1 h and their fits using a Guinier analysis. In inserts, the ln(I)=f(q^2) plots showing the linear domains.

A radius of gyration of 2.79±0.03 nm for the sample heat-treated at 575°C is obtained. This is larger than the radius of 1.56±0.06 nm obtained for the glass heat-treated at 550°C. This confirms a larger size of the scattering objects in the former sample, for which both XRD and ^{29}Si MAS-NMR reveal crystallization (Figure 3).

For the treatment at 550°C, with the hypothesis that in the early stages of crystallization the germs are spherical, it is possible to determine a sphere radius using the equation 6. A radius R=2.01±0.07 nm is determined, or a sphere diameter of 4.0±0.2 nm. It is also possible to fit the curve considering a form factor P(q) for a sphere (equation 7). The simulation is presented in Figure S7. The simulated radius is 1.89±0.06 nm, which is consistent with the Guinier's analysis. In the SANS analysis the scattering is ascribed to the LP phase since the contrast for the Li-silicate phases will not be very different to that of the glass matrix. This gives typical size for LP phase of 5 nm.

In order to determine the volume fraction of scattering objects, the contrast term $\Delta\rho^2 = \rho_{obj} - \rho_{medium}$ in equation 3 must be defined. For the surrounding medium, the SLD ρ_{medium}

is chosen equal to that of the glass. At 550°C, no crystalline phase is observed by XRD while a local rearrangement around P is observed using MAS-NMR, with the presence of disordered-LP species. It seems thus reasonable to consider the disordered-LP species as the scattering objects and the SLD can be approximated by considering that ρ_{obj} equals that of γ-Li_3PO_4. The real density of disordered-LP entities is smaller than the density of γ-Li_3PO_4 and the real SLD is thereby smaller. Consequently, the volume fraction values are overestimated. Details on the calculation of scattering length density for objects and the surrounding medium are presented in Table S3. A volume fraction of Φ_{obj}=4.9±0.4% is obtained. This small fraction explains the difficulty to observe such heterogeneities using TEM (Figure S4).

3.3.2 ^{31}P-^{31}P DQ-DRENAR

^{31}P-^{31}P DQ-DRENAR experiments were carried out on the LAS0.2-P1 as-cast glass and samples heat-treated at 550°C/1 h and 900°C/1 h. The latter one has been studied because phosphorus is entirely in the crystallized form Li_3PO_4. ^{31}P-^{31}P DQ-DRENAR curves are presented in Figure 7.

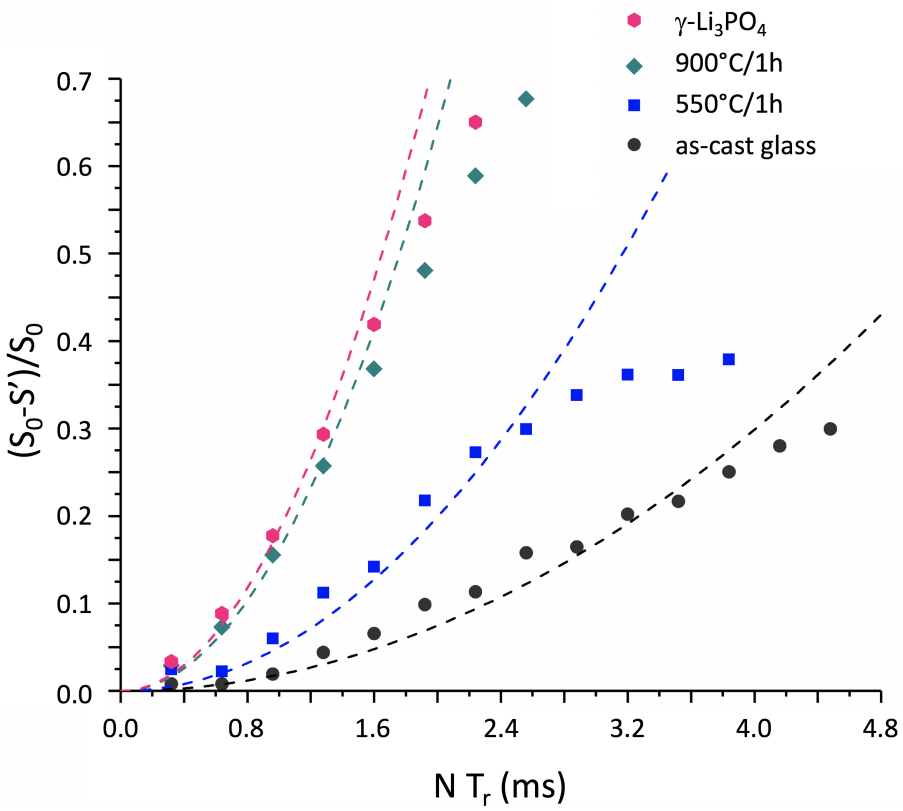

Figure 7: DQ-DRENAR curves for the as-cast glass LAS0.2-P1 (black circles), for the samples heat-treated at 550°C/1 h (blue squares) at 900°C/1 h (green diamonds) and for the crystalline reference γ-Li_3PO_4 (rose hexagons). N represents the cycle number for the measurement and T_r the rotation period (B_0=9.4 T, ν_{rot}=12.5 kHz). For each spectra S' and S_0, 32 accumulations have been obtained. In dashed lines, simulations at low NT_r values for the different sites for $\frac{S_0-S'}{S_0}$<0.30.

The amorphous and crystalline Q^0 species have no P-O-P bonds. The measurement of dipolar coupling constants ^{31}P-^{31}P DQ-DRENAR is thereby reflecting the spatial distribution of these species.[29] The data were measured on the peak located at ca. 9.3 ppm for the as-cast glass and the sample treated at 550°C/1h, as presented in a previous publication.[16] Note that for the latter glass, the contribution at 10 ppm assigned to the disordered-LP species and the glass contribution at 9.3 ppm, assigned to Q^0(0Al) species, are not distinguished in the DQ-DRENAR measurements.

For the sample heat-treated at 900°C/1h, the main peak corresponds to the Li_3PO_4 crystalline phase observed at 10.3 ppm. For comparison, we reported in Figure 7 the crystalline reference γ-Li_3PO_4 with a chemical shift at 9.6 ppm.[31] The curves in Figure 7 were fitted

using equation (1) for $\frac{S_0-S'}{S_0}$<0.30. The fit is shown as dashed lines and the fitted parameters are reported in Table 6. The dipolar constants are proportional to the interactions of the ^{31}P-^{31}P pairs in the system. Their values are close to those reported by Ren and Eckert[29] for glasses and crystalline references. They increase continuously when the temperature of the heat-treatment increases. The $\sum_k d_{jk}^2$ value for the as-cast glass is much lower than that of γ-Li_3PO_4. Following Ren and Eckert, this difference results from the greater dispersion of phosphorus atoms within the glass. Indeed, the dipolar coupling constants are lower because of the small amount of P_2O_5 in the glass and, if the P units are well dispersed, this induces very little proximity and therefore a small $\sum_k d_{jk}^2$ value. At 550°C, there is an increase in the $\sum_k d_{jk}^2$ value, which is intermediate between the as-cast glass and the treatment at 900°C. This evolution indicates that segregation of P occurs at this temperature.

Table 6: Experimental determination of the dipolar coupling constants $\sum_k d_{jk}^2$ (±10%) obtained from ^{31}P-^{31}P DQ-DRENAR experiments.

Sample	$\sum_k d_{jk}^2$x10^5 Hz^2 ±10%
LAS0.2-P1 as-cast glass	0.33
LAS0.2-P1 550°C/1h	0.89
LAS0.2-P1 900°C/1h	2.9
γ-Li_3PO_4	3.3

3.3.3 Isothermal changes at 525°C

DQ DRENAR indicates that P atoms are close to each other (Figure 7) at 550° C and a change in the ^{31}P NMR spectrum is observable after 1 h heat-treatment (Figure 4) at 550° C but modifications in the P environment appear also at 525° C . We therefore investigated the evolution with time for samples heat-treated at 525°C for 1 h (previously presented) and for 4 h. For this long heat-treatment, the sample is still XRD amorphous (figure 8a) and transparent.

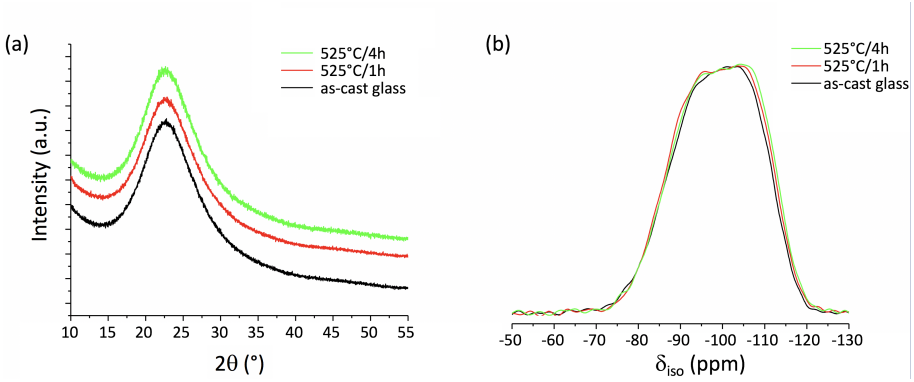

Figure 8: (a) X-ray diffractograms and (b) ^{29}Si MAS-NMR spectra of the as-cast glass LAS0.2-P1 and the samples heat-treated at 525°C for 1 h and 4 h.

Figure 8b shows the ^{29}Si NMR spectra. No resonances attributed to crystalline phases are observed. The features are slightly displaced towards more negative chemical shifts with longer duration of heat treatment, which could imply a reorganization of the glassy network. This remains uncertain given the small shift, but can be considered in view of the evolution of the ^{31}P MAS-NMR spectrum (see below) that clearly indicates a local reorganization of P atoms within the glass.

The ^{31}P MAS-NMR spectra of the heat treatments at 525°C are presented in Figure 9 and the parameters of the various contributions obtained by the simulation are presented in Table 5.

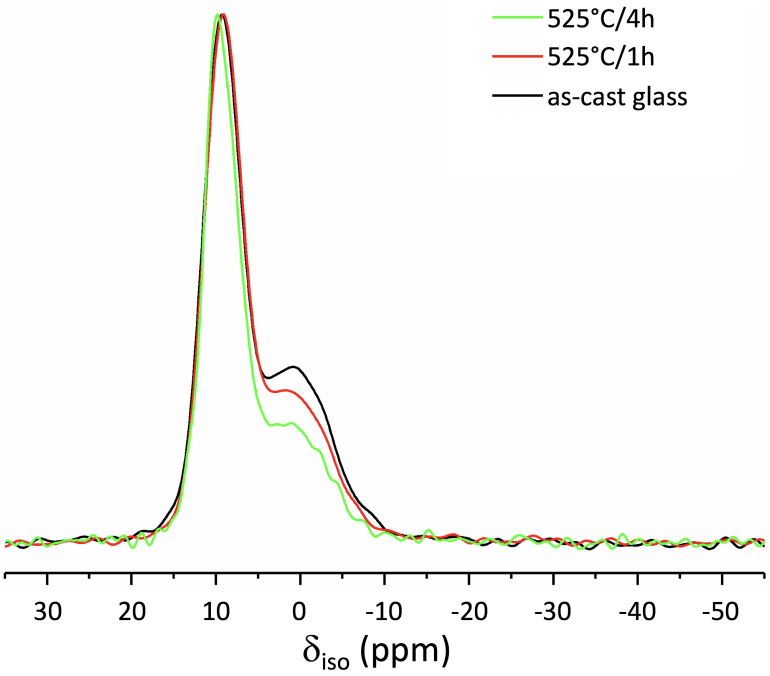

Figure 9: ^{31}P MAS-NMR spectra for the as-cast glass LAS0.2-P1 and for samples heat-treated at 525°C during 1 h and 4 h. The fitting parameters for the different contributions are detailed in Table 5.

There is an increase in the intensity of the disordered-LP contribution when the duration of the heat treatment is increased from 1 h to 4 h, with a decrease of the Q^1(0Al) contribution. For the treatment 525°C/4 h, 16% of the phosphorus atoms are in the form of disordered-LP species (close to the value obtained for the heating treatment at 550°C/1 h in Table 5).

Figure 11 compares the SANS patterns for the as-cast glass and the samples heat-treated at 525°C for 1 h and 4 h. There is a significant change in the SANS intensity after 4 h compared to the as-cast glass and the glass heat-treated at 525°C/1 h. A maximum appears at about 0.7 nm^{-1}, indicating a mesoscopic change in the glass organization.

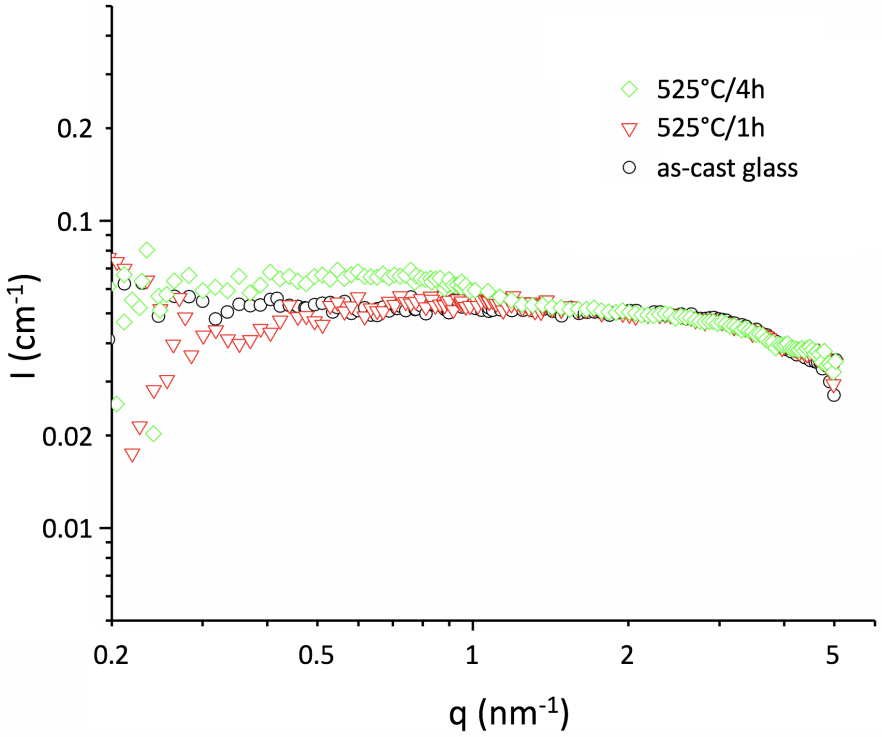

Figure 10: SANS curves for the as-cast glass LAS0.2-P1 and for samples heat-treated at 525°C during 1 h and 4 h. To improve curve readability, error bars are not shown but can be found in Figure S8.

A simulation using a sphere form factor model for the heat treatment 525°C/4 h (Figure S9) gives a sphere radius of 1.67±0.06 nm, i.e. a sphere diameter of 3.3±0.1 nm. This can be compared to the size previously obtained for the sample heat treated at 550°C/1 h (3.8±0.2 nm). To estimate the volume fraction of the objects, we used the SLD of the as-cast glass for the surrounding medium, and that of $\gamma - Li_3PO_4$ for the objects (Table S3). A volume fraction Φ_{obj} of 6.5±0.6% is obtained.

4 Discussion

4.1 Structural modification prior nucleation

In the LAS0.2-P1 glass composition, phosphorus is mostly in orthophosphate species surrounded by lithium ions, but isolated from the aluminosilicate network. SANS curves do not show compositional fluctuations, confirming that the phosphate species are well dispersed within the glass, as revealed by ^{31}P-^{31}P DQ-DRENAR experiments. Finally, TEM observations are unable to detect heterogeneities. Therefore, we conclude that P atoms are introduced in depolymerized, dispersed sites within the glass structure with no phase separation or compositional heterogeneities at the mesoscopic scale.

Slightly above Tg (Tg=508±1°C for LAS0.2-P1 glass)[16], the first structural modifications upon heating treatments appear at 525°C/1 h with a reorganization of the P environment involving the formation of disordered-LP entities at the expense of the Q^0(0Al) and Q^1(0Al) units. However, no mesoscopic effects are discernible by SANS or XRD, indicating that this structural reorganization is mainly local.

The amount of disordered-LP entities increases at 550°C, which can help to interpret changes at medium range distances detected by DQ-DRENAR and SANS measurements. The $\sum_k d_{jk}^2$ value is higher for the sample heat-treated at 550°C/1 h compared to the as-cast glass and it increases further for the glass heat-treated at 900°C/1 h. The simulation for the latter sample gives a $\sum_k d_{jk}^2$ value of 2.9x10^5 Hz^2, which is close to that obtained for the γ-Li_3PO_4 reference. This confirms the presence of Li_3PO_4 crystals after the treatment at 900°C/1 h, as observed by XRD and ^{31}P 1D-NMR.[16] For the glass heat-treated at 550°C/1 h, the value of the dipolar coupling constant increases compared to the value for the as-cast glass, from 0.33x10^5 Hz^2 to 0.89x10^5 Hz^2. This increase illustrates that orthophosphate entities are closer to each other at high temperature. However, the value remains lower than the crystalline Li_3PO_4 one. This is consistent with the formation of

disordered-LP species. This medium-range reorganization with a segregation of P species appears before any crystallization observable by XRD.

Ren and Eckert also studied the evolution of the $\sum_k d_{jk}^2$ dipolar constant values for different thermal treatments on a MKA glass sample (MKA glass: 66.9SiO_2-1.9Al_2O_3-28Li_2O-1.9K_2O-1.3P_2O_5)[29], previously studied by Bischoff et al..[14] They reported a value of 0.65x10^5 Hz^2. However, the selected thermal treatments did not reveal a significant difference in dipolar constant values for orthophosphates entities before the observation of crystallization of lithium metasilicate by XRD.

The evolution of the SANS signal can be explained by the segregation of P atoms within disordered-LP objects, for which sizes of about 4 nm in diameter are determined. An investigation using STEM-HAADF did not allowed the observation of a chemical contrast at 550°C/1 h (Figure 2b). In addition to the low chemical contrast in STEM-HAADF, this can be explained by the small volume fraction of objects (4.9% determined by SANS).

Changing the duration of the heat treatment induces similar changes than increasing the temperature of the heat treatment. A local rearrangement around phosphorus is observed in the ^{31}P MAS-NMR spectrum at 525°C/4 h, with 16% of the phosphorus atoms are in the form of poorly crystallized Li_3PO_4 (Figure 9, Table 5). This structural ordering is associated with a contrast in neutron scattering, with object sizes of about 3.3 nm in diameter. Similar to the heat treatment at 550°C/1 h, these areas are likely due to the disordered-LP entities.

4.2 Schematic scenario for nucleation

The as-cast glass is homogeneous and no heterogeneity is observed. Lithium orthophosphate (and pyrophosphate) species are well dispersed within the aluminosilicate network. Upon heating treatment, the nanoscale segregation of phosphate entities precedes the appearance of the crystalline phases observed at higher temperatures. These domains may correspond to amorphous or poorly organized regions composed of lithium orthophosphate groups, which act as seeds of crystallization for Li_3PO_4 crystals.[41]

Figure 11 illustrates the influence that the disordered-LP species can have on the volume crystallization of LAS0.2-P1 glass. The segregation of phosphate entities (stage 1) triggers the precipitation of Li_3PO_4 and leads to low-polymerized, Li-rich domains. These regions could be favourable to the crystallization of lithium metasilicate and disilicate (stage 2). The Li-rich areas could thus promote low interfacial energy between nuclei and glass, as mentioned by James for stoechiometric compositions of lithium disilicate.[5] Alternatively, the formation of disordered-LP allows the segregation of P atoms that are otherwise inhibiting crystallization when dispersed in the silicate network. It is not possible to assert at present whether the silicate phases appear in direct contact with Li_3PO_4 or whether they appear simultaneously with Li_3PO_4 or as a result of the formation of Li_3PO_4.

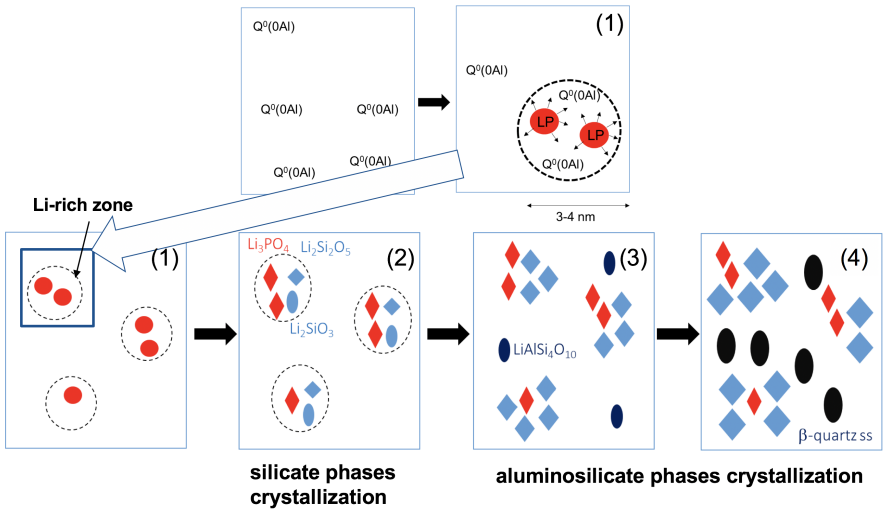

Figure 11: Schematic representation of the crystallization sequence of the glass LAS0.2-P1.

On the other hand, these Li-enriched domains that promote the appearance of lithium metasilicate and disilicate phases entail an impoverishment in lithium and an enrichment in aluminum of the residual glass. This residual glass, more polymerized, can thereby favors the crystallization of secondary phases containing aluminum, first petalite (stage 3) and eventually solid solution of β-quartz (stage 4).

It has been shown that the ability of ZrO_2 to nucleate magnesium aluminosilicate phases

can be related to the preferential arrangements between $Zr-O_x$ polyhedra, implying heterogeneities present in the as-cast glass.[2,3] Here in the composition LAS0.2-P1, P atoms show a preferential environment in the as-cast glass, but the phosphate entities appear homogeneously dispersed. A thermal treatment is required to compel the phosphate entities to segregate, confirming a heterogeneous mechanism for the first stages of nucleation.

5 Conclusions

XRD, SANS and NMR were used to investigate structural changes in a P_2O_5-Li_2O-Al_2O_3-SiO_2 glass, allowing local environments and mesoscale organization to be probed complementary. The glass containing 0.9% mol of P_2O_5 is homogeneous on a mesoscopic scale. No heterogeneities or segregation regions appear at 525°C/1 h on this scale. On the contrary, the local P environment evolves slightly as observed on ^{31}P MAS-NMR spectra. For treatments at 525°C/4 h and 550°C/1 h, where no crystallization is still observed by XRD, the local P rearrangement occurs concomitantly with changes at the mesoscopic scale revealed by SANS and ^{31}P-^{31}P DQ-DRENAR. Modifications of the P local environment are related to changes at the mesoscopic scale: the 3-4 nm zones observed by SANS can be associated with the first disordered Li_3PO_4 entities. This segregation develops with increasing time or increasing temperature. The evolution of P local environment and the segregation of phosphorus species precede the crystallization of the silicate and aluminosilicate phases, which are observed by XRD at higher temperature (575°C/1 h). P is thus playing an essential role in the initial stages of heat treatment by promoting nanoscale heterogeneities that allow a description of the crystallization mechanisms.

Acknowledgments

We would like to acknowledge the Characterization Science and Reliability group (CETC, Corning SAS). Thanks to Nicolas Menguy (IMPMC, Sorbonne Université) for TEM exper-

iments. The ANRT is acknowledged for PhD funding (P.G.) under the CIFRE Contract 2015/0529. The authors thank the Chevreul Institute (FR 2638) for its help in the development of this work. Chevreul Institute is supported by the "Ministère de l'Enseignement Supérieur et de la Recherche", the "Région Hauts-de-France" and the "Fonds Européen de Développement des Régions". This work benefited from the use of the SasView application, originally developed under NSF award DMR-0520547. SasView contains code developed with funding from the European Union's Horizon 2020 research and innovation programme under the SINE2020 project, grant agreement No 654000.

References

References

.

[1] Comte, M. From Glass to crystal - Nucleation, growth and phase separation, from research to applications; Science des Materiaux; EDP Sciences, 2017; pp 375–386.

[2] Dargaud, O.; Cormier, L.; Menguy, N.; Patriarche, G.; Calas, G. Mesoscopic scale description of nucleation processes in glasses. Appl. Phys. Lett. 2011, 99, 021904, DOI: 10.1063/1.3610557.

[3] Dargaud, O.; Cormier, L.; Menguy, N.; Patriarche, G. Multi-scale structuration of glasses: Observations of phase separation and nanoscale heterogeneities in glasses by Z-contrast scanning electron transmission microscopy. J. Non-Cryst. Solids 2012, 358, 1257–1262, DOI: 10.1016/j.jnoncrysol.2012.02.026.

[4] Kleebusch, E.; Patzig, C.; Höche, T.; Rüssel, C. The evidence of phase separation droplets in the crystallization process of a Li_2O-Al_2O_3-SiO_2 glass with TiO_2 as nucleating agent – An X-ray diffraction and (S)TEM-study supported by EDX-analysis. Ceramics International 2018, 44, 2919–2926, DOI: 10.1016/j.ceramint.2017.11.040.

[5] James, P.; Iqbal, Y.; Jais, U.; Jordery, S.; Lee, W. Crystallisation of silicate and phosphate glasses. Journal of Non-Crystalline Solids 1997, 219, 17–29, DOI: 10.1016/S0022-3093(97)00247-0.

[6] Höche, T.; Patzig, C.; Gemming, T.; Wurth, R.; Rüssel, C.; Avramov, I. Temporal

Evo- lution of Diffusion Barriers Surrounding $ZrTiO_4$ Nuclei in Lithia Aluminosilicate Glass-Ceramics. Cryst. Growth and Design 2012, 12, 1556–1563, DOI: 10.1021/cg2016148.

[7] Patzig, C.; Höche, T.; Dittmer, M.; Rüssel, C. Temporal evolution of crystallization in MgO-Al_2O_3-SiO_2-ZrO_2 glass ceramics. Crystal Growth Design 2012, 12, 2059–2067, DOI: 10.1021/cg3000334.

[8] Kleebusch, E.; Patzig, C.; Krause, M.; Hu, Y.; Höche, T.; Rüssel, C. The formation of nanocrystalline ZrO_2 nuclei in a Li_2O-Al_2O_3-SiO_2 glass – a combined XANES and TEM study. Scientific Reports 2017, 7, 10869.

[9] Maier, V.; Muller, G. Mechanism of Oxide Nucleation in Lithium Aluminosilicate Glass- Ceramics. Journal of the American Ceramic Society 1987, 70, C–176–C–178, DOI: 10.1111/j.1151-2916.1987.tb05717.x.

[10] Ananthanarayanan, A.; Kothiyal, G. P.; Montagne, L.; Tricot, G.; Revel, B. The effect of P_2O_5 on the structure, sintering and sealing properties of barium calcium aluminum boro-silicate (BCABS) glasses. Mater. Chem. Phys. 2011, 130, 880–889, DOI: 10.1016/j.matchemphys.2011.08.003.

[11]] Goswami, M.; Kothiyal, G. P.; Montagne, L.; Delevoye, L. MAS-NMR study of lithium zinc silicate glasses and glass-ceramics with various ZnO content. Journal of Solid State Chemistry 2008, 181, 269–275, DOI: 10.1016/j.jssc.2007.11.023.

[12] Headley, T.; Loehman, R. Crystallization of a Glass-Ceramic by Epitaxial Growth. Journal of the American Ceramic Society 1984, 67, 620–625, DOI: 10.1111/j.1151-2916.1984.tb19606.x.

[13] Holland, D.; Iqbal, Y.; James, P.; Lee, B. Early stages of crystallisation of lithium disilicate glasses containing P_2O_5 – An NMR study. Journal of Non-Crystalline Solids 1998, 232-234, 140–146, DOI: 10.1016/S0022-3093(98)00381-0.

[14] Bischoff, C.; Eckert, H.; Apel, E.; Rheinberger, V. M.; Höland, W. Phase evolution in lithium disilicate glass–ceramics based on non-stoichiometric compositions of a multi-component system: structural studies by ^{29}Si single and double resonance solid state NMR. Physical Chemistry Chemical Physics 2011, 13, 4540, DOI: 10.1039/c0cp01440k.

[15] Huang, S.; Zujovic, Z.; Huang, Z.; Gao, W.; Cao, P. Crystallization of a high-strength lithium disilicate glass-ceramic: An XRD and solid-state NMR investigation. Journal of Non-Crystalline Solids 2017, 457, 65–72, DOI: 10.1016/j.jnoncrysol.2016.11.015.

[16] Glatz, P.; Comte, M.; Cormier, L.; Montagne, L.; Doumert, B.; Moore, G. G. Different roles of phosphorus in the nucleation of lithium aluminosilicate glasses. Journal of Non- Crystalline Solids 2018, 493, 48–56, DOI: 10.1016/j.jnoncrysol.2018.04.021.

[17] James, P. F. Liquid-phase separation in glass-forming systems. J. Mater. Sc. 1975, 10, 1802–1825.

[18] Hill, R.; Calver, A.; Stamboulis, A.; Bubb, N. Real-Time Nucleation and Crystallization Studies of a Fluorapatite Glass-Ceramics Using Small-Angle Neutron Scattering and Neutron Diffraction. Journal of the American Ceramic Society 2007, 90, 763–768, DOI: 10.1111/j.1551-2916.2006.01474.x.

[19] Iqbal, Y.; Lee, W.; Holland, D.; James, P. Metastable phase formation in the early stage crystallisation of lithium disilicate glass. Journal of Non-Crystalline Solids 1998, 224,

1–16, DOI: 10.1016/s0022-3093(97)00453-5.

[20] Wright, A.; Fitch, A.; Hayter, J.; Fender, B. Crystallization of cordierite glass ceramic. part 1. Small angle neutron scattering measurement and simulation. Physics and Chem- istry of Glasses 1985, 26, 113–118.

[21] Lembke, U.; Brückner, R.; Kranold, R.; Höche, T. Phase Formation Kinetics in a Glass Ceramic Studied by Small-Angle Scattering of X-rays and Neutrons and by Visible-Light Scattering. Journal of Applied Crystallography 1997, 30, 1056–1064, DOI: 10.1107/S002188989700131

[22] Bras, W.; Greaves, G.; Oversluizen, M.; Clark, S.; Eeckhaut, G. The development of monodispersed alumino-chromate spinel nanoparticles in doped cordierite glass, studied by in situ X-ray small and wide angle scattering, and chromium X- ray spectroscopy. Journal of Non-Crystalline Solids 2005, 351, 2178–2193, DOI: 10.1016/j.jnoncrysol.2005.06.006.

[23] Fernandez-Martin, C.; Bruno, G.; Crochet, A.; Ovono Ovono, D.; Comte, M.; Hennet, L. Nucleation and Growth of Nanocrystals in Glass-Ceramics: An In Situ SANS Perspective. Journal of the American Ceramic Society 2012, 95, 1304–1312, DOI: 10.1111/j.1551-2916.2012.05093.x.

[24] Sigaev, V. N.; Golubev, N. V.; Ignat'eva, E. S.; Champagnon, B.; Vouagner, D.; Nar- dou, E.; Lorenzi, R.; Paleari, A. Native amorphous nanoheterogeneity in gallium germanosilicates as a tool for driving Ga2O3 nanocrystal formation in glass for optical devices. Nanoscale 2013, 5, 299–306.

[25] Donald, I. W.; Metcalfe, B. L.; Morris, A. E. P. Influence of transition metal oxide addi- tions on the crystallization kinetics, microstructures and thermal expansion character-

istics of a lithium zinc silicate glass. Journal of Materials Science 1992, 27, 2979–2999, DOI: 10.1007/BF01154109.

[26] Fayon, F.; Du ee, C.; Poumeyrol, T.; Allix, M.; Massiot, D. Evidence of Nanometric-Sized Phosphate Clusters in Bioactive Glasses As Revealed by Solid- State ^{31}P NMR. The Journal of Physical Chemistry C 2013, 117, 2283–2288, DOI: 10.1021/jp312263j.

[27] Mathew, R.; Turdean-Ionescu, C.; Stevensson, B.; Izquierdo-Barba, I.; Garcia, A.; Arcos, D.; Vallet-Regi, M.; Eden, M. Direct Probing of the Phosphate-Ion Distribution in Bioactive Silicate Glasses by Solid-State NMR: Evidence for Transitions be- tween Random/Clustered Scenarios. Chemistry of Materials 2013, 25, 1877–1885, DOI: 10.1021/cm400487a.

[28] Stevensson, B.; Mathew, R.; Eden, M. Assessing the Phosphate Distribution in Bioactive Phosphosilicate Glasses by 31P Solid-State NMR and Molecular Dynamics Simulations. The Journal of Physical Chemistry B 2014, 118, 8863–8876, DOI: 10.1021/jp504601c.

[29] Ren, J.; Eckert, H. Applications of DQ-DRENAR for the structural analysis of phosphate glasses. Solid State Nuclear Magnetic Resonance 2015, 72, 140–147, DOI: 10.1016/j.ssnmr.2015.10.009

[30] Massiot, D.; Fayon, F.; Capron, M.; King, I.; Le Calve, S.; Alonso, B.; Durand, J. O.; Bujoli, B.; Gan, Z. H.; Hoatson, G. Modelling one- and two-dimensional solid-state NMR spectra. Mag. Res. Chem. 2002, 40, 70–76.

[31] Glatz, P.; Comte, M.; Montagne, L.; Doumert, B.; Cormier, L. Quantitative determination of the phosphorus environment in lithium aluminosilicate glasses using solid-state NMR techniques. Physical Chemistry Chemical Physics 2019, 21, 18370–18379, DOI: 10.1039/C9CP03181B.

[32] Ren, J.; Eckert, H. DQ-DRENAR: A new NMR technique to measure site-resolved magnetic dipole-dipole interactions in multispin-1/2 systems: Theory and validation on crystalline phosphates. The Journal of Chemical Physics 2013, 138, 164201, DOI: 10.1063/1.4801634.

[33] Hohwy, M.; Jakobsen, H. J.; Eden, M.; Levitt, M. H.; Nielsen, N. C. Broadband dipolar recoupling in the nuclear magnetic resonance of rotating solids: A compensated C7 pulse sequence. The Journal of Chemical Physics 1998, 108, 2686–2694, DOI: 10.1063/1.475661.

[34] Cousin, F. Small angle neutron scattering. EPJ Web of Conferences 2015, 104, 01004, DOI: 10.1051/epjconf/201510401004.

[35] Glatter, O.; Kratky, O. Small angle x-ray scattering; Academic Press, 1982.

[36] Lelong, G.; Price, D. L.; Saboungi, M.-L. In Nanoporous Materials: Advanced Techniques for Characterization, Modeling, and Processing; Kanellopoulos, N., Ed.; CRC PressINC, 2011; pp 3–52.

[37] Benedetti, A.; Geotti-Bianchini, F.; Fagherazzi, G.; Riello, P.; Albertini, G.; De Riu, L. SAXS study of the micro-inhomogeneity of industrial soda lime silica glass. Journal of Non-Crystalline Solids 1994, 167, 263–271, DOI: 10.1016/0022-3093(94)90249-6.

[38] Kim, K. D.; Lee, S. H.; Hwang, J. H.; Seo, W. S. Nucleation behavior and microstructure of Al_2O_3-poor LAS glass–ceramics. Journal of Materials Science 2007, 42, 10180– 10187, DOI: 10.1007/s10853-007-1983-1.

[39] MacKenzie, K. J. D.; Smith, M. E. Multinuclear solid-state NMR of inorganic

materials; Pergamon materials series 6; Pergamon, 2002.

[40] de Jong, B. H. W. S.; Super, H. T. J.; Spek, A. L.; Veldman, N.; Nachtegaal, G.; Fischer, J. C. Mixed Alkali Systems: Structure and ^{29}Si MASNMR of Li_2Si_2O and $K_2Si_2O_5$. Acta Crystallographica Section B Structural Science 1998, 54, 568–577, DOI: 10.1107/S0108768198001062.

[41] Glatz, P. Influence de P_2O_5 sur la structure et la nucleation de verres d'aluminosilicates d'alcalins. PhD thesis, Sorbonne University 2018.

Supplementary Materials

element	coherent scattering length (fm)
Li	-1.90
P	5.13
Si	4.1491
Al	3.449
O	5.803

Table S1: Coherent neutron scattering lengths at q=0, from [Sears, V.F., Neutron Scattering Lengths and Cross Sections, *Neutron News*, 3 (1992) 26-37].

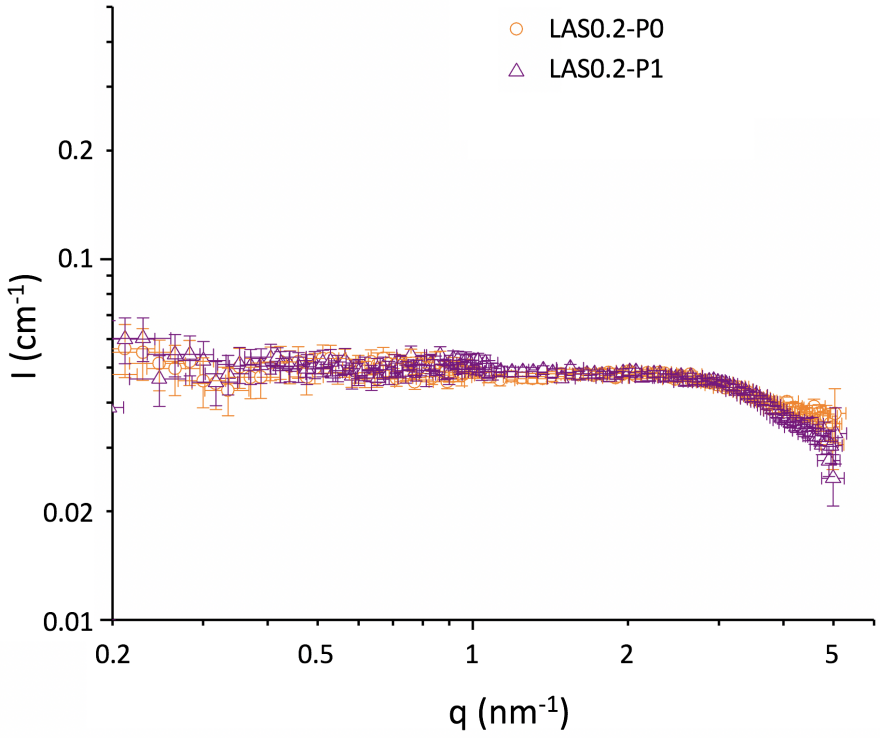

Figure S1: SANS curves with error bars for the glasses without P_2O_5 (LAS0.2-P0) and with P_2O_5(LAS0.2-P1).

	Li_2SiO_3	$Li_2Si_2O_5$
mol% SiO_2 analyzed	74.6	74.6
Molar weight glass ($g.mol^{-1}$)	57.8	57.8
Molar weight crystalline phase ($g.mol^{-1}$)	89.9657	150.0500
% of Si within crystals determined by spectra fitting	2	3
mol% crystalline phases	1.5 (2*74.6/100)	1.1 (3*(74.6/2)/100)
weight% crystalline phases	2.3 (1.5*89.9657/57.8)	2.9 (1.1*150.0500/57.8)

Table S2: Calculation of weight% of lithium metasilicate and disilicate phases obtained by fitting of ^{29}Si NMR spectra for the glass heat treated at 575°C/1h.

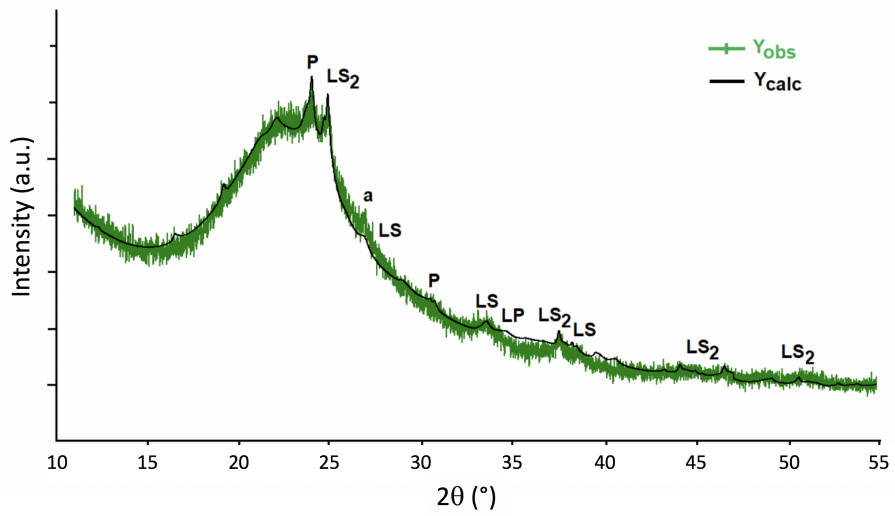

Figure S2: Comparison of observed (green) and calculated by Rietveld refinement (black) X-ray diffractograms obtained for LAS0.2-P1 heat-treated during 1 hour at 575°C. LS2: $Li_2Si_2O_5$, LS: Li_2SiO_3, P:$LiAlSi_4O_{10}$, a: α-quartz et LP: Li_3PO_4.

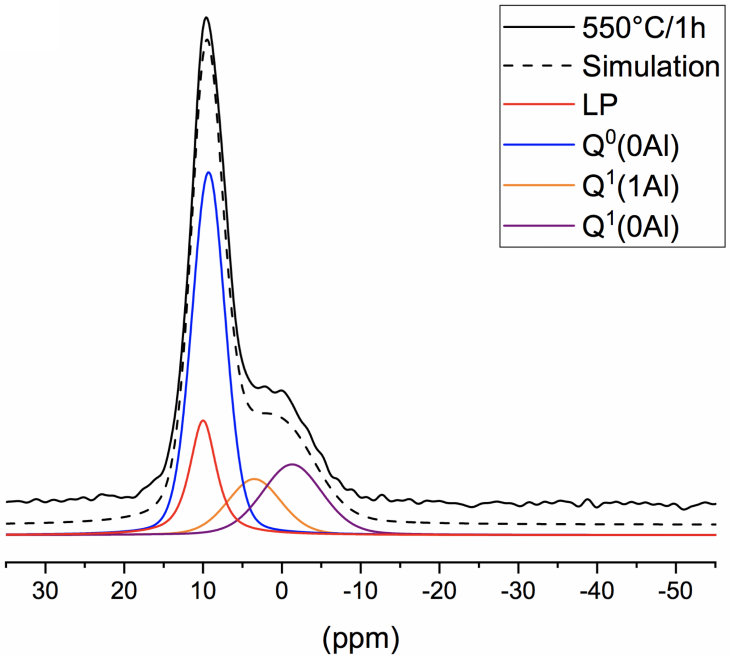

Figure S3: Typical fit of a ^{31}P MAS-NMR spectrum for the the LAS0.2-P1 glass after heat-treatment at 550°C during 1 hour

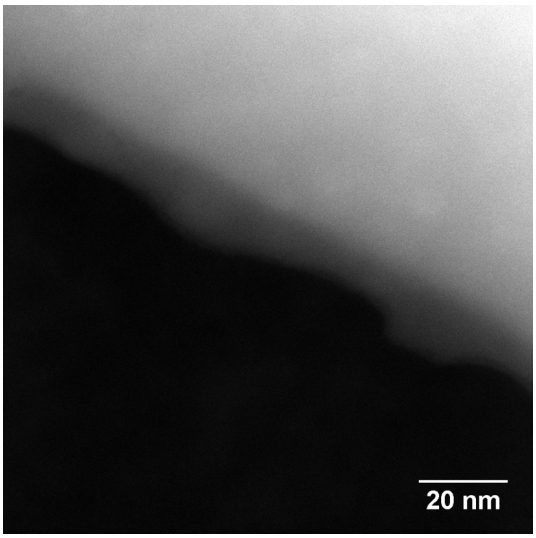

Figure S4: STEM-HAADF image of the LAS0.2-P1 sample after heat-treatment at 550°C during 1 hour.

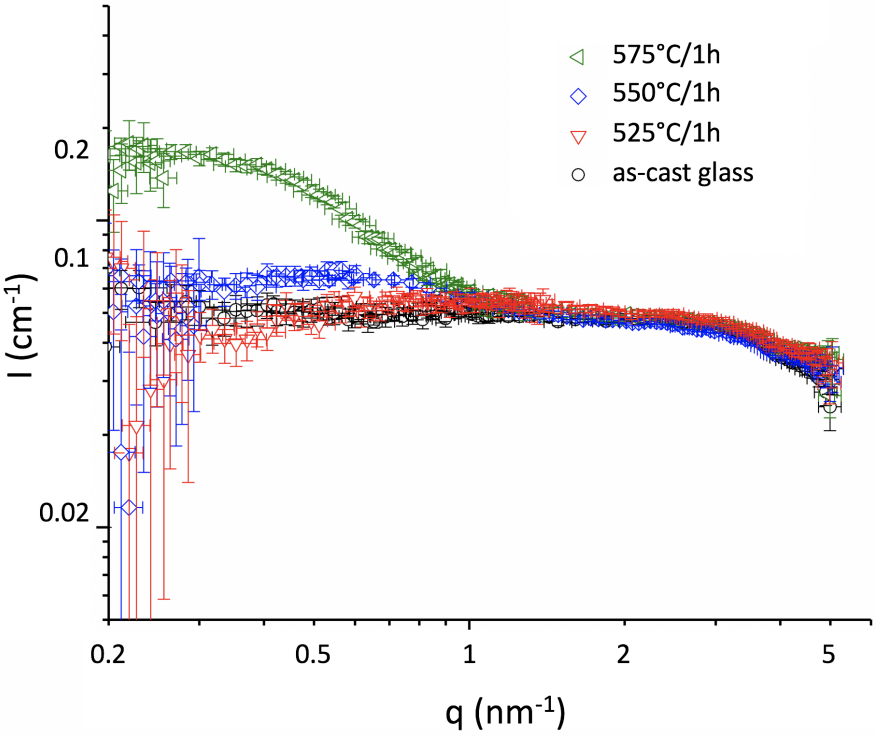

Figure S5: SANS curves with error bars for the as-cast glass LAS0.2-P1 and for samples heat-treated during 1 hour at various temperatures.

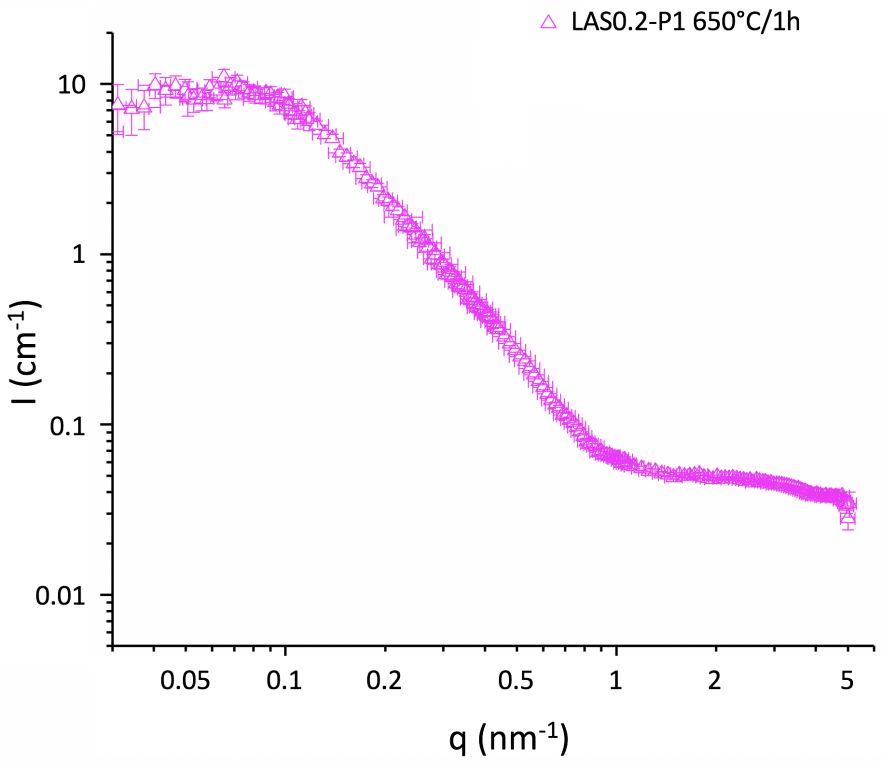

Figure S6: SANS curves with error bars for the LAS0.2-P1 heat-treated at 650°C/1 h.

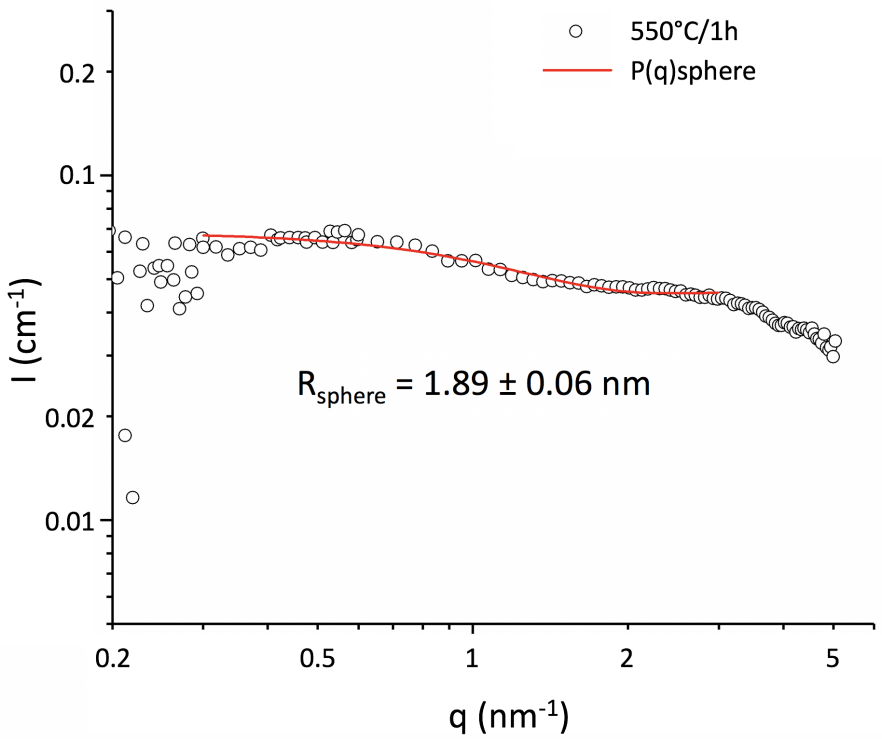

Figure S7: SANS curve with error bars for LAS0.2-P1 heat-treated at 550°C/1 h, compared with a fit using sphere form factor from q=0.3 to q=3 nm^{-1}.

	scattering elements	medium
	Li_3PO_4	LAS0.2-P1
density μ (g.cm^3)	2.429[a]	2.319[b]
molar weight M (g.mol^{-1})	115.456	57.776
$\nu = \frac{M}{\mu.Na}$ (Å^3)	78.959	41.371
b_{coh} ($\sum_i^n bi$) x10^{-5} (Å)	22.630	13.545
scattering length density $\rho(\frac{\sum_i^n bi}{\nu})$ x10^{-6} (nm^{-2})	**286.6**	**327.4**

Table S3: Calculation of scattering length density for the scattering objects and the surrounding medium for the fit using a sphere form factor for the glass heat-treated at 550°C/1 h. Na: Avogadro number [a] Calculated from the structure of γ-Li_3PO_4 JCPDS 00-015-0760. [b] Measurement by pycnometry, using a gaz Accu Pyc 1340 pycnometer from Micromeritics.

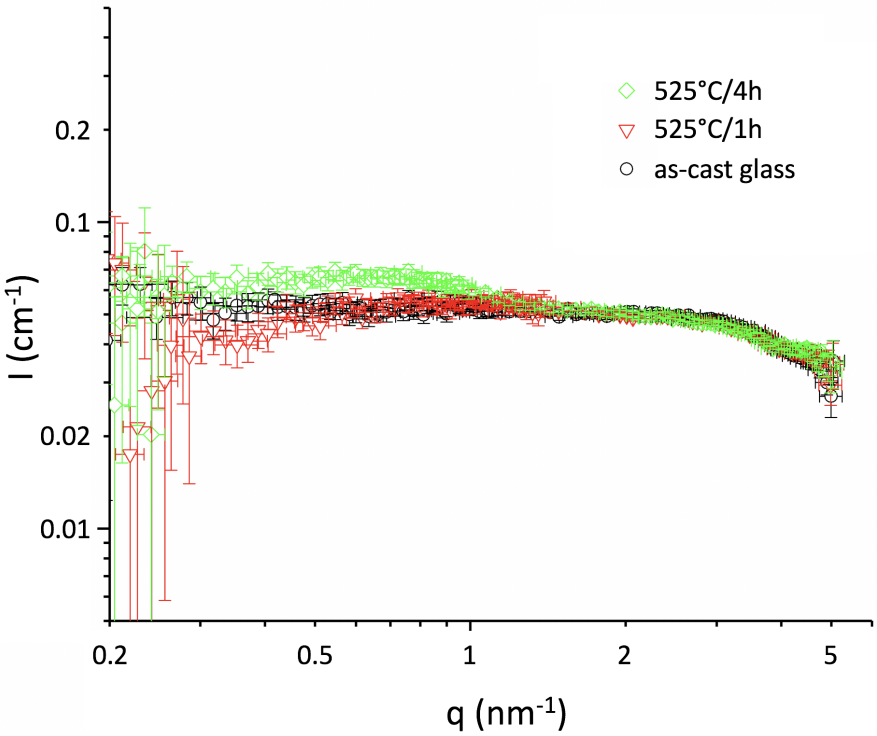

Figure S8: SANS curves with error bars for the as-cast glass LAS0.2-P1 and for samples

heat-treated at 525°C during 1 h and 4 h.

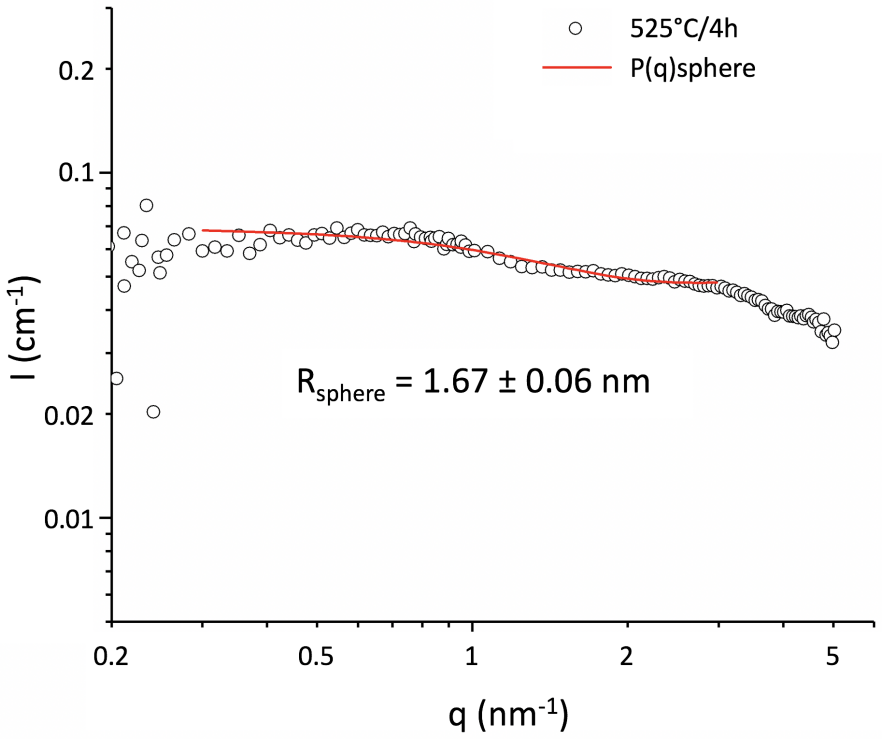

Figure S9: SANS curve for the as-cast glass LAS0.2-P1 heat-treated at 525°C/4 h, compared with the fit using a sphere form factor.